ACS MATERIALS LETTERS

www.acsmaterialsletters.org

Thermal Transport of Amorphous Hafnia Across the Glass Transition

Published as part of ACS Materials Letters special issue "Machine Learning for Materials Chemistry".

Zezhu Zeng,* Xia Liang, Zheyong Fan, Yue Chen, Michele Simoncelli, and Bingqing Cheng*

Cite This: *ACS Materials Lett.* 2025, 7, 2695–2701

ABSTRACT: Heat transport in glasses over a wide temperature range is critical for applications in gate dielectrics and thermal insulators but remains poorly understood due to the challenges in modeling vibrational anharmonicity and configurational dynamics across the glass transition. Recent predictions show an unusual decrease in thermal conductivity (κ) with temperature in amorphous hafnia (a-HfO_2), contrasting with the typical trend in glasses. Using molecular dynamics with a machine-learning-based neuroevolution potential, we compute κ of a-HfO_2 from 50 K to 2000 K. At low temperatures, the Wigner transport equation captures both anharmonicity and quantum statistics. Above 1200 K, atomic diffusion invalidates the quasiparticle picture, and we resort to the Green−Kubo method to capture convective transport. We further extend the Wigner transport equation to supercooled a-HfO_2, revealing the crucial role of low-frequency modes in facilitating heat transport. The computed κ, based on both Green−Kubo and Wigner transport theories, increases continuously with temperature up to 2000 K.

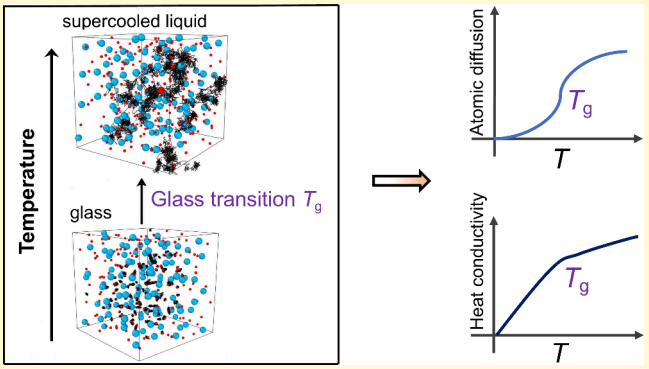

Understanding the thermal conductivity (κ) of glasses across the glass transition is crucial for applications such as electronic devices,[1] thermal barrier coatings,[2] and nuclear industries.[3] However, the heat transport mechanisms in glasses, from cryogenic to extremely high temperatures, remain poorly understood; unlike crystals, glasses lack long-range atomic ordering and the typical phonon picture breaks down.[4]

Experimentally, reported κ for glasses are often constrained to thin films,[5,6] as films are easier to vitrify due to faster cooling rates, compared to bulk glass in preparation, and high-temperature thermal measurements[7] are challenging, limiting data to small systems and narrow temperature ranges. For example, measurements of κ for glass a-SiO_2[5,6] span from 50 K to 1200 K, which remains below its glass transition temperature of ∼1500 K.[8]

Computationally, previous studies have mainly used molecular dynamics (MD) with empirical force fields, such as Beest−Kramer−Santen[9] and Tersoff[10] potentials for a-SiO_2, and Stillinger−Weber[9,11] and Tersoff[12] potentials for a-Si. While efficient, these potentials lack quantum mechanical accuracy, resulting in apparent deviations from experiments.[13] Ab initio molecular dynamics (AIMD)[14] offers higher precision, but it is limited to small systems and short time scales, making it particularly improper for complex amorphous systems. Recently, machine learning potential (MLP)[15] has emerged as a promising alternative, delivering density functional theory (DFT)-level accuracy with high computational efficiency. For example, Sivaraman et al.[16,17] developed a Gaussian approximation potential (GAP)[18] for amorphous HfO_2 (a-HfO_2), enabling large-scale MD simulations with nearly quantum mechanical precision.

Another computational challenge lies in developing accurate theories for computing and understanding the κ of glasses. The well-known Allen−Feldman theory[21,22] neglects vibrational anharmonicity. The Green−Kubo method, combined with MD simulations, can capture full-order anharmonicity but fails to account for quantum Bose−Einstein statistics. Recently, advanced methods within the lattice dynamics (LD) framework, such as the Wigner transport equation (WTE)[23−25] and

Received: February 7, 2025
Revised: June 17, 2025
Accepted: June 20, 2025
Published: June 30, 2025

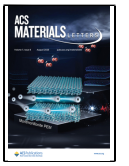

https://doi.org/10.1021/acsmaterialslett.5c00263
ACS Materials Lett. 2025, 7, 2695−2701

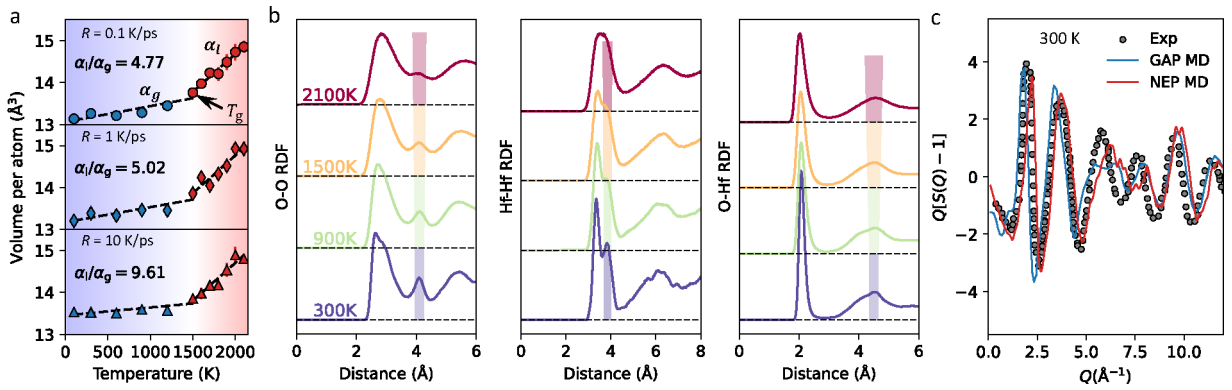

Figure 1. (a) Temperature dependence of the volume per atom for a-HfO_2 prepared at three quench cooling rates (R = 0.1, 1, and 10 K/ps). (b) Radial distribution functions (RDFs) for different atomic pairs (O−O, Hf−Hf, and O−Hf), calculated from NEP MD simulations at temperatures ranging between 300 K and 2100 K. (c) X-ray structure factors computed from NEP MD simulations, and the comparison with previous GAP MD simulations[16] and experiment.[19]

its regularization (rWTE),[26] as well as quasi-harmonic Green−Kubo (QHGK) theories[27,28] with hydrodynamic extrapolation,[29] have been developed to compute κ in finite-size models of disordered materials accounting for anharmonicity, structural disorder, and Bose−Einstein statistic of vibrations. These methods open doors for reliably studying glass heat transport, including a-SiO_2[24] (25−1200 K), a-Al_2O_3[30] (50−700 K), and a-Si[27] (50−1200 K). However, these studies are limited to temperatures below the glass transition. The exploration of κ in glasses across the glass transition remains in its infancy.

In this work, we focus on a-HfO_2, renowned for its excellent thermal stability[17] and applications in resistive random-access memory.[31] Using MLP MD simulations, we computed its dynamical and heat transport behaviors from 50 K to 2000 K, covering its glass-transition temperature near 1500 K. Understanding its thermal and dynamical properties is critical for ensuring the stability and reliability in advanced applications. In addition, a previous study,[20] based on QHGK theory, reported an decrease of computed κ in a-HfO_2 with increasing temperature, contrasting the typical trend of κ increasing or plateauing in glasses, warranting further investigation. We first trained a MLP based on the neuroevolution potential (NEP) approach,[32,33] using the training set from Sivaraman et al.[16,17] This dataset consists of 3682 configurations, including liquid-phase HfO_2 at 3600 K, amorphous HfO_2 at 300 K, as well as intermediate configurations sampled during the quenching process from 3600 K to 300 K. We prepared the structures of a-HfO_2 by by using a melt−quench−anneal process in NEP MD simulations, and then characterized their structure and vibrational properties across its glass-transition temperature. We then computed its κ over a wide range of temperatures, by using Green−Kubo theory, as well as by applying and extending rWTE.[26]

We first prepared glass structures in simulations. The melt−quench method in MD is commonly used to generate glass structures,[34] although the simulated cooling rate (1−10 K/ps) is much higher than the experimental rate (∼10 K/s), often yielding higher-energy, nonequilibrium structures. Particle swap Monte Carlo methods[35,36] can offer improved equilibration by accelerating phase space sampling with nonlocal moves, but are limited to the application of polydisperse systems due to the extremely low acceptance rates in ionic materials like a-HfO_2. Therefore, we stick to the melt−quench−anneal method for preparing the initial structures (see Notes S1 and S2 in the Supporting Information (SI) for a convergence test on the cooling rate R used). As detailed in the SI, we found that the computed κ in a-HfO_2 is insensitive to the quench rate used.

We then estimated the glass-transition temperature (T_g) by calculating the volume thermal expansion, as its derivative has a distinct jump near T_g in glass-forming materials.[37,38] Figure 1a shows the volume thermal expansion of a-HfO_2 from 100 K to 2100 K at three cooling rates, with a shift in temperature dependence around 1500 K, indicating the glass transition. We performed NEP MD simulations using a 756-atom supercell under the NPT ensemble, gradually heating the system from 100 K to 2100 K. At each temperature, the average volume was extracted from the equilibrium stage, and the volume per atom was calculated by dividing the average volume by the number of atoms. Below 1500 K, thermal expansion shows weaker temperature dependence, while above this temperature and below the melting point ($T_m \approx 3100$ K[17]), a supercooled liquid forms. Recently, Lunkenheimer et al.[38] observed that the ratio of the volume thermal expansion coefficient in the supercooled liquid (α_l) to that in the glass (α_g) is consistently ∼3 across 200 glassy materials with T_g values from 200 K to 1100 K. Interestingly, our simulations show that this ratio in a-HfO_2, α_l/α_g, decreases with lower cooling rates (i.e., closer to real cooling rates). At R = 0.1 K/ps, we find α_l/α_g = 4.8, approaching the reported ratio of 3 and extending the universal expansion law[38] to a-HfO_2 with a higher $T_g \approx 1500$ K.

Radial distribution functions (RDFs) illustrated in Figure 1b further reveal the structural evolution of a-HfO_2. Short-range order is reflected by the first RDF peaks at approximately 2.1 and 3 Å, while medium-range order is associated with the secondary peaks located at ∼4−5 Å. At low temperatures (e.g., 300 K), the O−Hf RDF features a sharp first peak at ∼2 Å, reflecting strong local bonding between O and Hf. The Hf−Hf RDF displays two distinct peaks at 3.39 Å and 3.87 Å, corresponding to edge-sharing and corner-sharing polyhedra,[16,19] respectively. The X-ray structure factor at 300 K further highlights typical glass characteristics, showing short-range order and long-range disorder in the atomic arrangements. As shown in Figure 1c, sharp and well-defined peaks at low scattering vector Q (e.g., the first peak around $Q \simeq 2.2$ Å^{-1}) indicate strong short-range correlations between neighboring atoms. At larger Q (e.g., Q > 5.0 Å^{-1}), the peaks become broader and weaker, reflecting a loss of coherence in atomic positions over longer distances, i.e., the

https://doi.org/10.1021/acsmaterialslett.5c00263
ACS Materials Lett. 2025, 7, 2695−2701

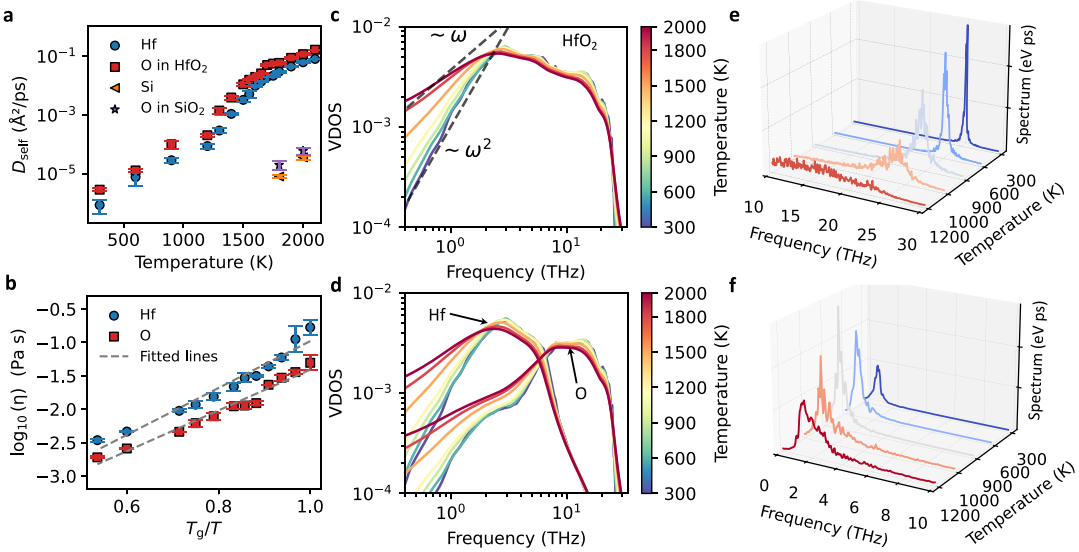

Figure 2. (a) Atomic self-diffusion coefficients (D) of hafnium (Hf) and oxygen (O) in a-HfO_2, and silicon (Si) and oxygen in a-SiO_2, computed from the velocity autocorrelation function in NEP MD simulations. (b) Logarithmic viscosity, $\log_{10}(\eta)$, as a function of T_g/T for Hf and O in a-HfO_2. Error bars represent uncertainties with dashed lines indicating linear fits. (c) Temperature-dependent vibrational density of states (VDOS) of a-HfO_2 with respect to frequency (ω) was calculated from NEP MD simulations. The dashed lines indicate the ω^2 scaling typical of solids and the ω scaling characteristic of liquids. (d) Projected VDOS for the Hf and the O elements. (e) Temperature-dependent power spectrum of the highest frequency mode. (f) The nonzero lowest frequency mode at the Γ point for a-HfO_2.

absence of long-range periodicity typical of glasses. The good agreement of structure factors from our NEP MD simulations with experimental data[19] and previous GAP MD simulations[16] further confirms the reliability of our NEP model.

As the temperature increases to 900 K, these glassy structure features at 300 K remain discernible, although a slight broadening occurs due to increased thermal motion. At 1500 K, near the glass transition, the medium-range structural order begins to break down. The O−O RDF, which initially shows a distinct second peak (see the trapezoid colorbar in Figure 1b) indicating medium-range ordering, gradually loses definition and disappears at 2100 K. Similarly, the split Hf−Hf peaks merge into a single broad peak at 2100 K. This loss of structure, along with the broadening of all RDF features, marks the collapse of medium-range order and the transition to a liquid-like state, reflecting increased atomic diffusion and structural rearrangement.

To understand the dynamics of the glass transition, we examined the self-diffusion coefficients, D_{self}, for Hf and O in a-HfO_2 (Figure 2a). As the temperature rises to 1200 K, D_{self} for both elements increases significantly. In a-HfO_2, oxygen diffuses slightly faster than hafnium, consistent with previous MD results based on an empirical potential.[39] Additionally, a-HfO_2 exhibits much higher diffusion in the supercooled liquid state than a-SiO_2 at 1800 and 2000 K, suggesting its enhanced atomic mobility. Note that the diffusion in supercooled liquid HfO_2 remains lower than in liquid HfO_2 (0.52 $Å^2$/ps for O and 0.24 $Å^2$/ps for Hf from DFT calculations[40]) at 3100 K. Figure 2b shows the viscosity behavior, essential for understanding glass flow and stability near T_g.[41] The viscosity, calculated via the Stokes−Einstein relation (see the SI for details), follows a linear trend with $\log_{10}(\eta)$ versus T_g/T, suggesting a strong glass behavior with stable structural dynamics across T_g, in contrast to the abrupt changes seen in fragile glass.[41]

To better understand frequency-dependent atomic dynamics, we computed the vibrational density of states (VDOS) of a-HfO_2 (see Figures 2c and 2d) from velocity autocorrelation functions. The most pronounced changes occur in the low-frequency (0−3 THz) region, and no distinct temperature difference is observed in the higher-frequency regions. At low temperatures (such as 300 K), the VDOS approaches a quadratic scaling relation ($\sim\omega^2$) in the low-frequency regime (below 0.8 THz, see the dashed line in Figure 2c), and displays a mild excess from such Debye scaling (boson peak) around 1 THz. As the temperature increases, the dependence transitions from ω^2 to a linear relationship. Notably, across the T_g, the VDOS in the low-frequency region becomes linear, a hallmark of liquid-like vibrational behavior,[42] reflecting a fundamental shift in the dynamics from solid to liquid states. The projected VDOS (Figure 2d) for different elements further elucidates the vibrational contributions: Hf atoms dominate the low-frequency vibrations due to their higher mass and stronger influence on collective acoustic-like modes, while the atoms of O dominate the high-frequency region, associated with localized vibrational modes. This elemental partitioning reflects the distinct roles of Hf and O in shaping the vibrational properties and heat transport in a-HfO_2.

To further evaluate the impact of atomic diffusion on vibrational mode decay, we computed the power spectrum using the normal mode decomposition method[43,44] (see Note S1 in the SI). In Figure 2e, we show the power spectrum of the highest-frequency mode in a-HfO_2 from 300 K to 1200 K. Significant broadening occurs with rising temperature, and at 1200 K, the typical Lorentzian profile is heavily disrupted. As a result, vibrational frequencies and line widths become ill-defined, indicating that lattice dynamics methods fail to compute κ due to the breakdown of the quasiparticle picture. Conversely, the lowest-frequency mode (Figure 2f) remains well-defined, even at 1200 K, where atomic diffusion occurs. Low-frequency, phonon-like modes near the Brillouin zone center show greater resilience to breakdown, similar to the robust transverse acoustic modes in superionic conductor $AgCrSe_2$[45] with Ag diffusion.

https://doi.org/10.1021/acsmaterialslett.5c00263
ACS Materials Lett. 2025, 7, 2695−2701

We now discuss the κ and heat transport mechanisms in a-HfO_2. Zhang et al.[20] trained a NEP model[32,33] using the training set from Sivaraman[16] and computed the κ of a-HfO_2 from 100 K to 2000 K using MD simulations and QHGK approach. They reported an unusual trend: κ continuously decreases with rising temperature above 900 K (see the dashed line in Figure 3b). This behavior contrasts with conventional

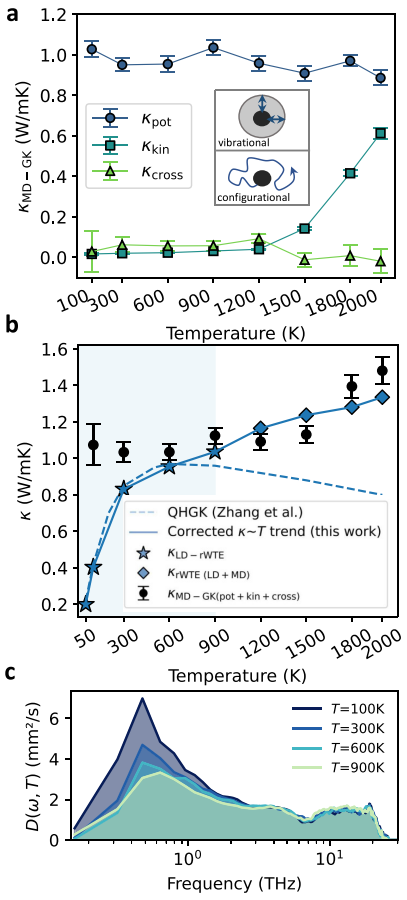

Figure 3. (a) Temperature dependence of the MD-GK thermal conductivities components for a-HfO_2: potential (κ_{pot}), kinetic (κ_{kin}), and cross (κ_{cross}) contributions. The inset panel illustrates the vibrational dynamics (localized vibration indicated by blue double-headed arrows) of a single atom and its configurational dynamics (diffusion indicated by a red solid line). (b) Comparison of the corrected κ−T trend (this work) with the QHGK model from Zhang et al.,[20] showing κ as a function of temperature. The corrected κ trend includes results from LD-rWTE ($\kappa_{LD-rWTE}$) and combined extended rWTE ($\kappa_{rWTE\ (LD+MD)}$). The shaded blue region indicates the temperature range in which rWTE is applicable (negligible atomic diffusion). (c) Frequency-dependent thermal diffusivity $D(\omega, T)$ computed at temperatures from 100 K to 900 K.

amorphous materials such as a-Si[9,46−49] and a-SiO_2,[5,6,10,50,51] where both experimental and calculated κ increases or saturates with rising temperature. Because Zhang et al.[20] focused on the heat conduction of a-HfO_2 and consider only the three-phonon line width of modes in the QHGK method, potential contributions from heat convection and effects of quasiparticle breakdown are not addressed.

We first investigated the critical role of heat convection in a-HfO_2 beyond the glass transition. Figure 3a presents the temperature-dependent conductivity, κ_{MD-GK}, of a-HfO_2 from Green−Kubo theory using NEP MD simulations (see Note S2 in the SI for computational details). The thermal conductivities were computed from 15 independent simulation runs. Given the isotropic nature of glassy a-HfO_2 (see Figure S5 and Table S1 in the SI for computed thermal conductivities at 300 K from Green−Kubo theory along the three Cartesian directions), the reported thermal conductivity values were obtained by numerically averaging the results along the x-, y-, and z-directions. κ_{MD-GK} is divided into three components: κ_{pot} is the conduction via atomic localized vibrations near equilibrium (vibrational dynamics;[38] see the inset of Figure 3a), κ_{kin} represents the convection due to atomic diffusion (configurational dynamics[38]), and κ_{cross} is the cross term between potential and kinetic terms. At low temperatures, κ_{pot} dominates, and κ_{kin} and κ_{cross} are negligible. However, as the temperature approaches T_g, κ_{kin} rises sharply, underscoring the role of convection originated from the atomic diffusion in the supercooled liquid state. In Figure 3b, we show the κ_{MD-GK} (black circle dots) from 100 K to 2000 K. At high temperatures, κ_{MD-GK} increases due to convective contributions, contrasting with the QHGK κ reported by Zhang et al.[20] As the temperature approaches zero, κ_{MD-GK} remains constant, in contrast to the decreasing trend observed in QHGK results. This reflects limitation of classical MD in lacking nuclear quantum effects, leading to constant heat capacity instead of the quantum-reduced values in real materials. At high temperatures, classical Green−Kubo theory may overestimate κ in materials with significant mass flow such as superionic conductors[52] or multicomponent systems.[53] A more rigorous treatment using Onsager relations[53,54] could improve the accuracy of calculated κ from MD simulations.

To address these limitations, we employed the rWTE[26] to calculate κ (see Note S2 in the SI for details) from 50 K to 900 K, as it can intrinsically account for the quantum (Bose−Einstein) distribution of atomic vibrations. The rWTE method accelerates the convergence of κ calculations in strongly disordered solids, where disorder-induced repulsion between vibrational energy levels[55] is comparable to the intrinsic line width caused by anharmonicity or isotopes. In such systems, line widths primarily enable vibrational mode coupling, with minimal impact on the computed κ. Examples include a-SiO_2[26] and a-Al_2O_3.[30] The rWTE can be written as[26]

$$\kappa = \frac{1}{\mathcal{V}N_c}\sum_{\mathbf{q},s,s'}\frac{\omega(\mathbf{q})_s+\omega(\mathbf{q})_{s'}}{4}\left(\frac{C(\mathbf{q})_s}{\omega(\mathbf{q})_s}+\frac{C(\mathbf{q})_{s'}}{\omega(\mathbf{q})_{s'}}\right)\frac{\|\mathbf{v}(\mathbf{q})_{s,s'}\|^2}{3} \times \pi\mathcal{F}_{[\Gamma(\mathbf{q})_s+\Gamma(\mathbf{q})_{s'},\eta]}(\omega(\mathbf{q})_s-\omega(\mathbf{q})_{s'}) \quad (1)$$

where $\mathcal{V}$ is the simulation cell volume, N_c the number of $\mathbf{q}$-points, s and s' are band indices, ω the vibrational frequency, $C(\mathbf{q})s$ the quantum-based specific heat, $\mathbf{v}(\mathbf{q})s$, s' the velocity operator, and Γ the line width. The Voigt distribution $\mathcal{F}_{[\Gamma(\mathbf{q})s+\Gamma(\mathbf{q})s',\eta]}$ results from convolving a Lorentzian (width $\Gamma(\mathbf{q})s + \Gamma(\mathbf{q})s'$) with a Gaussian (variance $\eta^2\pi/2$). Due to the prohibitive computational cost of rigorously calculating vibrational line widths in atom-heavy primitive cells for glasses, we employed a coarse-grained, frequency-dependent single-valued line width function, following established strategies from previous studies to reduce computational complexity. The actual line widths at the Γ point, computed via normal-mode decomposition and used to fit this single-valued function, inherently include full-order anharmonic effects. Additionally, we validated this approach by comparing thermal

https://doi.org/10.1021/acsmaterialslett.5c00263
ACS Materials Lett. 2025, 7, 2695−2701

conductivities obtained from the rWTE method using a 3 × 3 × 3 **q**-mesh interpolation with those computed from the WTE at **q** = **0**, finding no significant differences (see Figure S10 in the SI).

As shown in Figure 3b, the rWTE κ increases with temperatures from 50 K to 900 K, consistent with experimental observations for many glasses, and it also aligns well with the QHGK results.[20] It also agrees with our bare WTE κ, calculated using a 6144-atom unit cell at **q** = 0 (see Figure S10 in the SI), demonstrating that rWTE can reliably evaluate the heat conduction in a-HfO_2 with strong atomic disorder.[56] Above 900 K, significant atomic diffusion causes a breakdown of the quasiparticle picture (Figure 2e), rendering LD-based methods like rWTE and QHGK invalid as they both require well-defined frequencies and line widths for vibrations. Thus, these methods are applicable only in solids where atomic diffusion is negligible and quasi-particle vibrational excitations are well-defined.

To shed light on the microscopic mechanisms underlying convective transport at higher temperatures, we phenomenologically employed the WTE framework for supercooled liquid a-HfO_2. Under the hypothesis that the conductivity of a supercooled liquid can be described by a mathematical expression analogous to that emerging from the WTE, we rewrite eq 1 into the equivalent form $\kappa = \frac{1}{\mathcal{V}N_c}\sum_{\mathbf{q},s} C(\mathbf{q})_s D(\mathbf{q})_s$, where $D(\mathbf{q})_s$ represents the anharmonic thermal diffusivity, defined as[26]

$$D(\mathbf{q})_s = \sum_{s'} \frac{\omega(\mathbf{q})_s + \omega(\mathbf{q})_{s'}}{2[\Gamma(\mathbf{q})_s + \Gamma(\mathbf{q})_{s'}]}\left[\frac{C(\mathbf{q})_s}{\omega(\mathbf{q})_s} + \frac{C(\mathbf{q})_{s'}}{\omega(\mathbf{q})_{s'}}\right]\frac{\|\mathbf{v}(\mathbf{q})_{ss'}\|^2}{3} \times \pi\mathcal{F}_{[\Gamma(\mathbf{q})_s+\Gamma(\mathbf{q})_{s'},\eta]}(\omega(\mathbf{q})_s - \omega(\mathbf{q})_{s'}) \quad (2)$$

To directly compare LD and MD properties, it is informative to express diffusivity as a function of frequency. Thus, we recast the $D(\mathbf{q})_s$ as a frequency-dependent function as $D(\omega,T) = [g(\omega)\mathcal{V}N_c]^{-1} \times \sum_{\mathbf{q},s} D(\mathbf{q})_s \delta(\omega - \omega(\mathbf{q})_s)$, where $g(\omega)$ represents the VDOS (Figure 2c). The frequency-dependent quantities defined above allow to rewrite the rWTE κ in frequency space as

$$\kappa(T) = \int_0^\infty g(\omega)C(\omega, T)D(\omega, T)\,\mathrm{d}\omega \quad (3)$$

In classical MD simulations at high temperatures, $C(\omega,T)$ becomes temperature-independent and approaches the Boltzmann constant k_B. Practically, $D(\omega,T)$ also remains nearly temperature-independent in a-HfO_2 at these temperatures. This may be attributed to the interplay between the low-frequency VDOS and the velocity operator, where an increase in one (Figure 2c) is offset by a decrease in the other, resulting in nearly temperature-independent diffusivity. Our calculations from 100 K to 900 K (Figure 3c) reveal minimal differences for $D(\omega,T)$ above 600 K, suggesting that the increase in κ in supercooled liquid a-HfO_2 likely results from the enhanced low-frequency VDOS. Additionally, due to $D(\omega,T)$ has a peak at the low-frequency region, which gives rise to a potentially critical contribution related to low-frequency modes. We confirm this by integrating the thermal diffusivity from lattice dynamics at 900 K with the temperature-dependent VDOS from MD simulations (Figure 2c) at higher temperatures by using eq 3. As shown in Figure 3b, the integrated κ (κ_{LD+MD}) successfully reproduces the $\kappa_{MD\text{-}GK}$ results above 900 K. This agreement improves our understanding of heat transport across the glass transition in amorphous materials, where the enhanced low-frequency VDOS (dominated by relatively heavy atoms, such as Hf in a-HfO_2) plays a key role in increasing κ. From the Green−Kubo perspective within MD, this enhancement arises from heat convection, while the rWTE within the LD framework highlights the crucial role of low-frequency propagating modes in enhancing convection in supercooled liquid a-HfO_2. Although mode diffusivity $D(\omega,T)$ slightly decreases with increasing temperature (see Figure 3c), the overall thermal conductivity still rises due to the significant enhancement of low-frequency vibrational states and corresponding modal heat capacities at elevated temperatures. Thus, despite the reduced diffusivity, the integrated effect leads to a net increase in thermal conductivity at high temperatures.

Through MLP MD simulations, we unveiled the glass transition and structural evolution in a-HfO_2, where significant atomic diffusion across the glass transition emerges as a crucial factor shaping the thermal transport. Using the Green−Kubo theory, we quantified the considerable heat convection in a-HfO_2. We further extended the WTE method to offer new insights into microscopic heat transport mechanisms within the supercooled liquid state. Our findings reveal a continuous increase in κ of a-HfO_2 with temperature up to 2000 K. This work deepens understanding of structural transitions and heat transport in amorphous materials, and it may pave the way for future research in superionic,[45] disordered,[57] and supercooled systems.

■ ASSOCIATED CONTENT

Data Availability Statement

All necessary source data files generated for this study are available in the GitHub repository https://github.com/ZengZezhu/heat-conductivity-a-HfO2.

Supporting Information

The Supporting Information is available free of charge at https://pubs.acs.org/doi/10.1021/acsmaterialslett.5c00263.

Calculation details for machine learning potential construction,[59,60] molecular dynamics simulations, and thermal conductivity evaluation based on the Green−Kubo theory and the Wigner transport equation,[61−63] including convergence tests for thermal conductivity calculations. (PDF)

■ AUTHOR INFORMATION

Corresponding Authors

Zezhu Zeng − *The Institute of Science and Technology Austria, 3400 Klosterneuburg, Austria;* orcid.org/0000-0001-5126-4928; Email: u3004964@connect.hku.hk

Bingqing Cheng − *Department of Chemistry, University of California, Berkeley, California 94720, United States; The Institute of Science and Technology Austria, 3400 Klosterneuburg, Austria;* orcid.org/0000-0002-3584-9632; Email: bingqingcheng@berkeley.edu

Authors

Xia Liang − *Department of Materials, Imperial College London, South Kensington Campus, London SW7 2AZ, United Kingdom;* orcid.org/0000-0002-9351-1082

Zheyong Fan − *College of Physical Science and Technology, Bohai University, Jinzhou 121013, China;* orcid.org/0000-0002-2253-8210

https://doi.org/10.1021/acsmaterialslett.5c00263
ACS Materials Lett. 2025, 7, 2695−2701

Yue Chen − *Department of Mechanical Engineering, The University of Hong Kong, Hong Kong, SAR 999077, China*
Michele Simoncelli − *Theory of Condensed Matter Group, Cavendish Laboratory, University of Cambridge, Cambridge CB2 1TN, United Kingdom; Department of Applied Physics and Applied Mathematics, Columbia University, New York 10027, United States*

Complete contact information is available at: https://pubs.acs.org/10.1021/acsmaterialslett.5c00263

Notes

A preprint[58] of this work is available online.
The authors declare the following competing financial interest(s): B.C. has an equity stake in AIMATX, Inc.

■ ACKNOWLEDGMENTS

We thank Ludovic Berthier for fruitful discussions and Ting Liang for providing the initial structures of a-SiO_2. Z.Z. acknowledges funding from the European Union's Horizon 2020 Research and Innovation Programme, under Marie Skłodowska-Curie grant agreement No. 101034413. The authors also acknowledge the research computing facilities provided by HPC ISTA and ITS HKU.

■ REFERENCES

(1) Cahill, D. G.; Braun, P. V.; Chen, G.; Clarke, D. R.; Fan, S.; Goodson, K. E.; Keblinski, P.; King, W. P.; Mahan, G. D.; Majumdar, A.; et al. Nanoscale thermal transport. II. 2003−2012. *Appl. Phys. Rev.* **2014**, *1*, 011305.
(2) Qiu, J.-Y.; Montecillo, R.; Chen, P.-Y.; Tu, C.-S.; Chen, C.-S.; Fu, B.-R.; Feng, K.-C. Development of the Al2O3-B2O3-SiO2 glass for thermal barrier coating. *J. Non-Cryst. Solids* **2024**, *626*, 122785.
(3) Al-Buriahi, M. S.; Olarinoye, I.; Alomairy, S.; Kebaili, I.; Kaya, R.; Arslan, H.; Tonguc, B. T. Dense and environment friendly bismuth barium telluroborate glasses for nuclear protection applications. *Progress Nuclear Energy* **2021**, *137*, 103763.
(4) DeAngelis, F.; Muraleedharan, M. G.; Moon, J.; Seyf, H. R.; Minnich, A. J.; McGaughey, A. J.; Henry, A. Thermal transport in disordered materials. *Nanoscale Microscale Thermophys. Eng.* **2019**, *23*, 81−116.
(5) Cahill, D. G.; Pohl, R. O. Thermal conductivity of amorphous solids above the plateau. *Phys. Rev. B* **1987**, *35*, 4067.
(6) Cahill, D. G.; Ford, W. K.; Goodson, K. E.; Mahan, G. D.; Majumdar, A.; Maris, H. J.; Merlin, R.; Phillpot, S. R. Nanoscale thermal transport. *J. Appl. Phys.* **2003**, *93*, 793−818.
(7) Zhao, D.; Qian, X.; Gu, X.; Jajja, S. A.; Yang, R. Measurement techniques for thermal conductivity and interfacial thermal conductance of bulk and thin film materials. *J. Electron. Packaging* **2016**, *138*, No. 040802.
(8) Polian, A.; Vo-Thanh, D.; Richet, P. Elastic properties of a-SiO_2 up to 2300 K from Brillouin scattering measurements. *Europhys. Lett.* **2002**, *57*, 375.
(9) Larkin, J. M.; McGaughey, A. J. Thermal conductivity accumulation in amorphous silica and amorphous silicon. *Phys. Rev. B* **2014**, *89*, 144303.
(10) Lv, W.; Henry, A. Non-negligible contributions to thermal conductivity from localized modes in amorphous silicon dioxide. *Sci. Rep.* **2016**, *6*, 35720.
(11) Moon, J.; Latour, B.; Minnich, A. J. Propagating elastic vibrations dominate thermal conduction in amorphous silicon. *Phys. Rev. B* **2018**, *97*, No. 024201.
(12) Lv, W.; Henry, A. Direct calculation of modal contributions to thermal conductivity via Green−Kubo modal analysis. *New J. Phys.* **2016**, *18*, No. 013028.
(13) Zhang, H.; Wei, H.; Bao, H. Thermal Transport Mechanism of Amorphous HfO_2: A Molecular Dynamics Based Study. *J. Therm. Sci.* **2022**, *31*, 1052−1060.
(14) Car, R.; Parrinello, M. Unified approach for molecular dynamics and density-functional theory. *Physical review letters* **1985**, *55*, 2471.
(15) Deringer, V. L.; Caro, M. A.; Csányi, G. Machine learning interatomic potentials as emerging tools for materials science. *Adv. Mater.* **2019**, *31*, 1902765.
(16) Sivaraman, G.; Krishnamoorthy, A. N.; Baur, M.; Holm, C.; Stan, M.; Csányi, G.; Benmore, C.; Vázquez-Mayagoitia, Á. Machine-learned interatomic potentials by active learning: amorphous and liquid hafnium dioxide. *npj Comput. Mater.* **2020**, *6*, 104.
(17) Sivaraman, G.; Gallington, L.; Krishnamoorthy, A. N.; Stan, M.; Csányi, G.; Vázquez-Mayagoitia, Á.; Benmore, C. J. Experimentally driven automated machine-learned interatomic potential for a refractory oxide. *Phys. Rev. Lett.* **2021**, *126*, 156002.
(18) Bartók, A. P.; Payne, M. C.; Kondor, R.; Csányi, G. Gaussian approximation potentials: The accuracy of quantum mechanics, without the electrons. *Phys. Rev. Lett.* **2010**, *104*, 136403.
(19) Gallington, L. C.; Ghadar, Y.; Skinner, L. B.; Weber, J. R.; Ushakov, S. V.; Navrotsky, A.; Vazquez-Mayagoitia, A.; Neuefeind, J. C.; Stan, M.; Low, J. J.; et al. The structure of liquid and amorphous hafnia. *Materials* **2017**, *10*, 1290.
(20) Zhang, H.; Gu, X.; Fan, Z.; Bao, H. Vibrational anharmonicity results in decreased thermal conductivity of amorphous HfO_2 at high temperature. *Phys. Rev. B* **2023**, *108*, No. 045422.
(21) Allen, P. B.; Feldman, J. L. Thermal conductivity of glasses: Theory and application to amorphous Si. *Phys. Rev. Lett.* **1989**, *62*, 645.
(22) Allen, P. B.; Feldman, J. L. Thermal conductivity of disordered harmonic solids. *Phys. Rev. B* **1993**, *48*, 12581.
(23) Simoncelli, M.; Marzari, N.; Mauri, F. Unified theory of thermal transport in crystals and glasses. *Nat. Phys.* **2019**, *15*, 809−813.
(24) Simoncelli, M.; Marzari, N.; Mauri, F. Wigner formulation of thermal transport in solids. *Phys. Rev. X* **2022**, *12*, No. 041011.
(25) Caldarelli, G.; Simoncelli, M.; Marzari, N.; Mauri, F.; Benfatto, L. Many-body Green's function approach to lattice thermal transport. *Phys. Rev. B* **2022**, *106*, No. 024312.
(26) Simoncelli, M.; Mauri, F.; Marzari, N. Thermal conductivity of glasses: First-principles theory and applications. *npj Computational Materials* **2023**, *9*, 106.
(27) Isaeva, L.; Barbalinardo, G.; Donadio, D.; Baroni, S. Modeling heat transport in crystals and glasses from a unified lattice-dynamical approach. *Nat. Commun.* **2019**, *10*, 3853.
(28) Fiorentino, A.; Baroni, S. From Green−Kubo to the full Boltzmann kinetic approach to heat transport in crystals and glasses. *Phys. Rev. B* **2023**, *107*, No. 054311.
(29) Fiorentino, A.; Pegolo, P.; Baroni, S. Hydrodynamic finite-size scaling of the thermal conductivity in glasses. *npj Comput. Mater.* **2023**, *9*, 157.
(30) Harper, A. F.; Iwanowski, K.; Witt, W. C.; Payne, M. C.; Simoncelli, M. Vibrational and thermal properties of amorphous alumina from first principles. *Phys. Rev. Mater.* **2024**, *8*, No. 043601.
(31) Broglia, G.; Ori, G.; Larcher, L.; Montorsi, M. Molecular dynamics simulation of amorphous HfO_2 for resistive RAM applications. *Modell. Simul. Mater. Sci. Eng.* **2014**, *22*, No. 065006.
(32) Fan, Z.; Zeng, Z.; Zhang, C.; Wang, Y.; Song, K.; Dong, H.; Chen, Y.; Ala-Nissila, T. Neuroevolution machine learning potentials: Combining high accuracy and low cost in atomistic simulations and application to heat transport. *Phys. Rev. B* **2021**, *104*, 104309.
(33) Song, K.; Zhao, R.; Liu, J.; Wang, Y.; Lindgren, E.; Wang, Y.; Chen, S.; Xu, K.; Liang, T.; Ying, P.; et al. General-purpose machine-learned potential for 16 elemental metals and their alloys. *Nat. Commun.* **2024**, *15*, 10208.
(34) Deringer, V. L.; Bernstein, N.; Csányi, G.; Ben Mahmoud, C.; Ceriotti, M.; Wilson, M.; Drabold, D. A.; Elliott, S. R. Origins of structural and electronic transitions in disordered silicon. *Nature* **2021**, *589*, 59−64.

(35) Ninarello, A.; Berthier, L.; Coslovich, D. Models and algorithms for the next generation of glass transition studies. *Phys. Rev. X* **2017**, *7*, No. 021039.
(36) Berthier, L.; Reichman, D. R. Modern computational studies of the glass transition. *Nat. Rev. Phys.* **2023**, *5*, 102−116.
(37) Debenedetti, P. G.; Stillinger, F. H. Supercooled liquids and the glass transition. *Nature* **2001**, *410*, 259−267.
(38) Lunkenheimer, P.; Loidl, A.; Riechers, B.; Zaccone, A.; Samwer, K. Thermal expansion and the glass transition. *Nat. Phys.* **2023**, *19*, 694−699.
(39) Schie, M.; Müller, M. P.; Salinga, M.; Waser, R.; De Souza, R. A. Ion migration in crystalline and amorphous HfO_x. *J. Chem. Phys.* **2017**, *146*, DOI: 10.1063/1.4977453.
(40) Hong, Q.-J.; Ushakov, S. V.; Kapush, D.; Benmore, C. J.; Weber, R. J.; van de Walle, A.; Navrotsky, A. Combined computational and experimental investigation of high temperature thermodynamics and structure of cubic ZrO_2 and HfO_2. *Sci. Rep.* **2018**, *8*, 14962.
(41) Mauro, J. C.; Yue, Y.; Ellison, A. J.; Gupta, P. K.; Allan, D. C. Viscosity of glass-forming liquids. *Proc. Natl. Acad. Sci. U. S. A.* **2009**, *106*, 19780−19784.
(42) Zaccone, A.; Baggioli, M. Universal law for the vibrational density of states of liquids. *Proc. Natl. Acad. Sci. U. S. A.* **2021**, *118*, No. e2022303118.
(43) McGaughey, A. J.; Larkin, J. M. Predicting phonon properties from equilibrium molecular dynamics simulations. *Ann. Rev. Heat Transfer* **2014**, *17*, 49.
(44) Carreras, A.; Togo, A.; Tanaka, I. DynaPhoPy: A code for extracting phonon quasiparticles from molecular dynamics simulations. *Comput. Phys. Commun.* **2017**, *221*, 221−234.
(45) Ding, J.; Niedziela, J. L.; Bansal, D.; Wang, J.; He, X.; May, A. F.; Ehlers, G.; Abernathy, D. L.; Said, A.; Alatas, A.; et al. Anharmonic lattice dynamics and superionic transition in $AgCrSe_2$. *Proc. Natl. Acad. Sci. U. S. A.* **2020**, *117*, 3930−3937.
(46) Zink, B.; Pietri, R.; Hellman, F. Thermal conductivity and specific heat of thin-film amorphous silicon. *Physical review letters* **2006**, *96*, No. 055902.
(47) Feldman, J. L.; Kluge, M. D.; Allen, P. B.; Wooten, F. Thermal conductivity and localization in glasses: Numerical study of a model of amorphous silicon. *Phys. Rev. B* **1993**, *48*, 12589.
(48) Wang, Y.; Fan, Z.; Qian, P.; Caro, M. A.; Ala-Nissila, T. Quantum-corrected thickness-dependent thermal conductivity in amorphous silicon predicted by machine learning molecular dynamics simulations. *Phys. Rev. B* **2023**, *107*, No. 054303.
(49) Braun, J. L.; Baker, C. H.; Giri, A.; Elahi, M.; Artyushkova, K.; Beechem, T. E.; Norris, P. M.; Leseman, Z. C.; Gaskins, J. T.; Hopkins, P. E. Size effects on the thermal conductivity of amorphous silicon thin films. *Phys. Rev. B* **2016**, *93*, 140201.
(50) Zhu, X.; Shao, C. Effect of anharmonicity on the thermal conductivity of amorphous silica. *Phys. Rev. B* **2022**, *106*, No. 014305.
(51) Freeman, J. J.; Anderson, A. C. Thermal conductivity of amorphous solids. *Phys. Rev. B* **1986**, *34*, 5684−5690.
(52) Liu, W.; Zhou, Y. Energy Transport in Superionic Crystals. *Phys. Rev. Lett.* **2025**, *134*, 146301.
(53) Pegolo, P.; Drigo, E.; Grasselli, F.; Baroni, S. Transport coefficients from equilibrium molecular dynamics. *J. Chem. Phys.* **2025**, *162*, DOI: 10.1063/5.0249677.
(54) Bertossa, R.; Grasselli, F.; Ercole, L.; Baroni, S. Theory and numerical simulation of heat transport in multicomponent systems. *Phys. Rev. Lett.* **2019**, *122*, 255901.
(55) Simkin, M.; Mahan, G. Minimum thermal conductivity of superlattices. *Phys. Rev. Lett.* **2000**, *84*, 927.
(56) Iwanowski, K.; Csányi, G.; Simoncelli, M. Bond-Network Entropy Governs Heat Transport in Coordination-Disordered Solids. *arXiv Preprints*, arXiv:2412.12753 (accessed Dec. 17, 2024).
(57) Zeng, Z.; Fan, Z.; Simoncelli, M.; Chen, C.; Liang, T.; Chen, Y.; Thornton, G.; Cheng, B. Lattice distortion leads to glassy thermal transport in crystalline $Cs_3Bi_2I_6Cl_3$. *arXiv Preprints*, arXiv:2407.18510 (accessed July 26, 2024).
(58) Zeng, Z.; Liang, X.; Fan, Z.; Chen, Y.; Michele, S.; Cheng, B. Thermal transport of amorphous hafnia across the glass transition. *arXiv Preprints*, arXiv:2502.03114 (accessed Feb. 5, 2025).
(59) Liang, T.; Ying, P.; Xu, K.; Ye, Z.; Ling, C.; Fan, Z.; Xu, J. Mechanisms of temperature-dependent thermal transport in amorphous silica from machine-learning molecular dynamics. *Phys. Rev. B* **2023**, *108*, 184203.
(60) Fan, Z.; Wang, Y.; Ying, P.; Song, K.; Wang, J.; Wang, Y.; Zeng, Z.; Xu, K.; Lindgren, E.; Rahm, J. M.; et al. GPUMD: A package for constructing accurate machine-learned potentials and performing highly efficient atomistic simulations. *J. Chem. Phys.* **2022**, *157*, 114801.
(61) Togo, A.; Chaput, L.; Tanaka, I. Distributions of phonon lifetimes in Brillouin zones. *Phys. Rev. B* **2015**, *91*, No. 094306.
(62) Togo, A.; Chaput, L.; Tadano, T.; Tanaka, I. Implementation strategies in phonopy and phono3py. *J. Phys.: Condens. Matter* **2023**, *35*, 353001.
(63) Thebaud, S.; Berlijn, T.; Lindsay, L. Perturbation theory and thermal transport in mass-disordered alloys: Insights from Green's function methods. *Phys. Rev. B* **2022**, *105*, 134202.

https://doi.org/10.1021/acsmaterialslett.5c00263
ACS Materials Lett. 2025, 7, 2695−2701